Permeability of volcanic rocks to gas and water

M.J. Heap, T. Reuschlé, J.I. Farquharson, P. Baud

Permeability of volcanic rocks to gas and water

M. J. Heap*, T. Reuschlé, J. I. Farquharson, and P. Baud

Géophysique Expérimentale, Institut de Physique de Globe de Strasbourg (UMR 7516 CNRS, Université de Strasbourg/EOST), 5 rue René Descartes, 67084 Strasbourg cedex, France.

*Corresponding author: heap@unistra.fr

Highlights

- Gas permeability is a factor of 2-5 higher than water permeability in two volcanic rocks.
- The average pore radius (assuming tube-shaped pores) used by gas, calculated using the Klinkenberg slip factor, is ~0.1-0.5 μm.
- We speculate that the radius of these microstructural elements is restricted or that they are inaccessible to water due to water adsorption.
- A difference between water and gas permeability has important implications for fluid flow in volcanic systems.

Abstract

The phase (gas or liquid) of the fluids within a porous volcanic system varies in both time and space. Laboratory experiments have shown that gas and water permeabilities can differ for the same rock sample, but experiments are biased towards rocks that contain minerals that are expected react with the pore fluid (such as the reaction between liquid water and clay). We present here the first study that systematically compares the gas and water permeability of volcanic rocks. Our data show that permeabilities to argon gas and deionised water can differ by a factor between two and five in two volcanic rocks (basalt and andesite) over a confining pressure range from 2 to 50 MPa. We suggest here that the microstructural elements that offer the shortest route through the sample—estimated to have an average radius ~0.1-0.5 μm using the Klinkenberg slip factor—are accessible to gas, but restricted or inaccessible to water. We speculate that water adsorption on the surface of these thin microstructural elements, assumed here to be tortuous/rough microcracks, reduces their effective radius and/or prevents access. These data have important implications for fluid flow and therefore the distribution and build-up of pore pressure within volcanic systems.

Keywords: permeability; Klinkenberg; volcano; pore fluid; microstructure

1. Introduction

Permeability is a measure of the ability of a material to transmit fluids [*Guéguen and Palciauskas*, 1994]. The permeability of volcanic rocks therefore largely controls the movement of fluids and the distribution of pore pressure in a volcanic edifice. The build-up of pore pressure within a volcanic system is thought to promote explosive volcanism [e.g., *Eichelberger et al.*, 1986; *Sparks*, 1997; *Melnik et al*., 2005; *Farquharson et al.*, 2017] and flank collapse [e.g., *Reid*, 2004] and, as such, many experimental and theoretical studies have been devoted to better understanding the permeability of volcanic materials [e.g., *Eichelberger et al.*, 1986; *Saar and Manga*, 1999; *Blower*, 2001; *Rust and Cashman*, 2004; *Mueller et al.*, 2005; *Costa*, 2006; *Mueller et al.*, 2008; *Wright et al.*, 2009; *Degruyter et al.*, 2010; *Lavallée et al*., 2013; *Gaunt et al.*, 2014; *Farquharson et al.*, 2015, 2016; *Heap and Kennedy*, 2016; *Wadsworth et al.*, 2016; *Lindoo et al.*, 2016; *Heap et al.*, 2016, 2017; *Burgisser et al.*, 2017; *Kushnir et al*., 2017a; *Colombier et al*., 2017; *Vasseur and Wadsworth*, 2017; *Kushnir et al*., 2017b]. These studies, and many others, have shown that the permeability of volcanic materials is not only an increasing function of porosity (a scalar), but also highlight the importance of a wealth of additional parameters, such as porosity type (pores and microcracks), pore geometry (size, shape, and preferred orientation), porosity connectivity, and alteration, amongst others.

The constitutive equation that describes fluid flow through a porous medium is Darcy's law [*Darcy*, 1856]. The equation relates a volumetric flow rate to a fluid pressure gradient using a coefficient called the permeability. Permeability is a property of the medium and is therefore independent of the fluid used in its determination. Darcy's law is valid for all porous media as long as the volumetric flow rate is linearly proportional to the fluid pressure gradient, i.e. the flow is laminar. For instances of nonlaminar flow, auxiliary corrections are required to derive the "true" (Darcian) permeability of a medium from pressure and flow rate data. For example, when measuring materials with very high permeabilities and/or using pore fluids with very low viscosities, fluid flow can be turbulent. In this regime, a new parameter is introduced in order to account for inertial forces: this

is known as the Forchheimer correction [*Forchheimer*, 1901]. Another instance where the relationship between volumetric flow rate and fluid pressure gradient is nonlinear is specific to measurements using gas. When the mean free path of the molecules/atoms approaches the characteristic pore or aperture size, interactions between the gas molecules/atoms and the pore walls serve to reduce resistance to flow, a phenomenon known as "slip flow" or "gas slippage". In this case, the apparent permeability is corrected using the Klinkenberg correction [*Klinkenberg*, 1941].

Most of the experimental studies designed to measure the permeability of volcanic rocks use an inert gas as the pore fluid; only a handful of studies have used water [e.g., *Kolzenburg et al.*, 2012; *Kendrick et al*., 2013; *Heap et al.*, 2014a, b; *Gaunt et al.*, 2014]. To the knowledge of the authors, there are no studies that compare gas and water permeabilities in volcanic materials. Laboratory measurements have shown that permeabilities to liquid water and gas are essentially equal for granite [*Brace et al*., 1968; *Zhang et al.*, 2000]. A difference between permeabilities to gas and water has been observed for rocks containing mineral constituents that can react with the pore fluid, such as the reaction between liquid water and clay [*Faulkner and Rutter*, 2000, 2003; *Tanikawa and Shimamoto* 2006; *Davy et al*., 2007; *Tanikawa and Shimamoto* 2009; *Behnsen and Faulkner*, 2011] or the reaction between CO_2-enriched water and calcite [*Noiriel et al*., 2004; *Luquot and Gouze*, 2009]. These studies have shown, for example, that permeabilities to gas and liquid water in clay-rich rocks can differ by as much as an order of magnitude [e.g., *Faulkner and Rutter*, 2000]. A higher permeability to gas in clay-rich rocks is explained by the expansion of clay minerals in the presence of water due to water adsorption – the swollen clay minerals effectively constrict pore throats thus reducing permeability [*Faulkner and Rutter*, 2003].

It is often assumed, after the appropriate corrections have been applied, that permeabilities to gas and water are equivalent for materials for which significant physicochemical reactions are not expected. However, a lack of data comparing the gas and water permeabilities of a range of materials obscures a complete understanding. For example, the complex microstructure presented by volcanic

rocks—often a complex network of pores and microcracks [*Heap et al.,* 2014a; *Farquharson et al*., 2015; *Colombier et al*., 2017]—may yield a difference in permeabilities to gas and water in the absence of significant physicochemical reactions. The phase (gas or liquid) of the fluids within a porous volcanic system varies in time and space [e.g., *Giggenbach and Soto*, 1992; *Taran et al*., 1998; *Chiodini et al*., 2000; *Byrdina et al.*, 2014], exemplified by the occurrence of phreatic and phreatomagmatic eruptions that are driven by the boiling of liquid water [e.g., *Houghton and Nairn*, 1991; *Barberi et al*., 1992; *Mayer et al*., 2015; *Montanaro et al*., 2016]. As a result, quantifying potential differences in the permeability to gas and water in volcanic rocks emerges as an important, yet unexplored, avenue for research. With this in mind, we present herein a study in which we measured the gas and water permeabilities of samples of andesite and basalt.

2. Description of experimental materials

For the purpose of this study, we selected a suite of variably porous andesites from Volcán de Colima (Mexico) and a well-studied basalt from Mt Etna (Italy). Volcán de Colima is an active andesitic stratovolcano located at the western end of the Trans-Mexican Volcanic Belt in Mexico [*Varley and Komorowski*, 2018] and Mt Etna is an active basaltic stratovolcano located on the east coast of the island of Sicily (Italy) [*Allard et al*., 2006].

The five andesite blocks used in this study (A5, B4, B5, C8, and LAH4) have been used in a number of recent studies focussed on the mechanical behaviour of andesite [e.g., *Kendrick et al*., 2013; *Heap et al.,* 2014a; 2015]. Using the classification scheme of *Farquharson et al*. [2015], sample B5 can be classified as an "altered lava" (B5 displays high-temperature alteration, as evidenced by the presence of cristobalite; Figure 1a), while the remaining blocks can be classified as "lava". The andesites all have a porphyritic texture consisting of a glassy groundmass (with abundant microlites) that hosts pores and a phenocryst cargo (Figure 1). The porosity within these andesites comprises a combination of microcracks and pores (Figure 1) [*Kendrick et al*., 2013; *Heap et al.,* 2014a; 2015]. As

evident in the scanning electron microscope (SEM) images of Figure 1, the andesites contain a microcrack network that is both pervasive and tortuous. Indeed, microcrack densities range between 35 and 45 mm^{-1} [*Heap et al.,* 2014a]. The microcracks are typically thin (no more than a few microns) and are usually no longer than 0.5 mm in length (Figure 1). The andesites also contain high pore number densities, between 3.3 and 8.1 mm^{-2} [*Heap et al.,* 2014a]. The pores are often far from spherical (Figure 1) and are, in the case of the lowest porosity sample (B5), coated with cristobalite crystals (Figure 1a). All of the andesites show a wide range of pore diameters, from 1-2 mm to a few tens of microns [*Heap et al.,* 2014a].

The basalt from Mt Etna has porphyritic texture consisting of a completely crystallised groundmass containing pores and a phenocryst cargo (Figure 2). This basalt has been the focus of a number of studies in the last ten years [e.g., *Vinciguerra et al*., 2005; *Stanchits et al*., 2006; *Heap et al*., 2011; *Zhu et al*., 2016]. The porosity within the basalt comprises a combination of microcracks and pores (Figure 2). Qualitatively, the microcracks in the basalt are typically much longer (often several mm) than those in the andesites (Figures 1 and 2). The microcracks within the basalt often traverse through both the crystallised groundmass and the large phenocrysts present within the sample (Figure 2a). The pores within the basalt are not distributed throughout the sample, but are present in pockets (Figure 2b). The pores within these porous pockets represent the volume between microlites where the groundmass is absent, a texture termed diktytaxitic [see, for example, *Kushnir et al*., 2016]. The pores are typically less than 100 microns in diameter (Figure 2b).

2. Experimental methods

Cylindrical samples (20 mm in diameter and precision-ground to a nominal length of 40 mm) were prepared from the five blocks of andesite (A5, B4, B5, C8, and LAH4) and the block of basalt. These samples were then dried in a vacuum oven at 40 °C for at least 48 h. Before measuring their permeability, the prepared 20 mm-diameter samples were first investigated in terms of their

connected porosity (using helium pycnometry) and specific surface area (using Brunauer, Emmett, and Teller (BET) gas adsorption measurements).

The connected porosity of each sample was measured using the skeletal (connected) volume provided by a helium pycnometer (Micromeritics AccuPyc II 1340) (values are an average of 20 measurements; precision ± 0.00005 cm^3) and the bulk volume determined using the sample dimensions (precision ± 0.005 mm). The specific surface area was determined using BET nitrogen or krypton adsorption measurements [*Brunauer et al*., 1938]. The samples were placed a vacuum sealed vessel (itself placed in a liquid nitrogen bath at a temperature of -196.15 °C) and the specific surface area was calculated by determining the amount of adsorbate gas needed to create a monomolecular layer on the connected surface inside the sample. The absorbent gas used for the basalt was nitrogen. Krypton gas was used for the andesite samples due to their low specific surface areas (krypton is better suited for samples with low specific surface areas due to its smaller molecular size). More details on the BET method and theory employed here can be found in *Brunauer et al*. [1938] and *Kushnir et al*. [2016].

To assess their pore throat structure, mercury injection porosimetry was performed on pieces (~5 g) of two of the andesite blocks (B5 and C8) and the basalt using the Micromeritics Autopore IV 9500 at the University of Aberdeen (Scotland). The evacuation pressure and evacuation time were 50 μmHg and 5 min, respectively, and the mercury filling pressure and equilibration time were 0.52 pounds per square inch absolute (psia) and 10 s, respectively. The pressure range was 0.1 to 60,000 psia (i.e. up to a pressure of about 400 MPa). Mercury injection data permit the calculation of the pore throat size distribution within a particular sample. The mercury injection data were corrected for the "low pressure correction" recommended by ASTM International [ASTM D4404-10].

The permeabilities to gas (argon) and water (deionised water) were then measured on the prepared cylindrical samples. We first performed a suite of gas and water permeability measurements on the variably porous andesite samples at a confining pressure of 2 MPa. We then

160 performed gas and water permeability measurements at a range of confining pressures (from 1 to 50
161 MPa) on a sample of andesite (B5) and a basalt sample. To avoid problems associated with potential
162 permanent microstructural changes following exposure to 50 MPa, we used different samples (cored
163 from the same block) for the gas and water permeability measurements in these latter experiments.
164 The pairs of samples for these experiments were selected based on their almost identical initial
165 permeabilities (measured with inert gas at a confining pressure of 1 MPa).

166 Samples to be measured with water were first vacuum-saturated with deionised water. The
167 saturation procedure consisted of three steps:

168 (1) the samples were vacuum-dried at 40 °C for at least 48 h,
169 (2) the samples were then immediately placed inside a belljar which was then vacuumed for
170 at least 12 h and, finally,
171 (3) degassed (using a Venturi siphon with municipal water as the motive fluid), deionised
172 water was introduced into the belljar (whilst under vacuum).

173 Great care was taken to ensure that the water was fully degassed and that the samples were fully
174 saturated. Once prepared, the samples were jacketed in a viton sleeve and placed inside a hydrostatic
175 pressure vessel. The confining pressure (P_c) was then increased to 2 MPa (for the set of
176 measurements on the variably porous andesite sample suite) or 1 MPa (for the measurements to be
177 performed at different confining pressures). The samples were left overnight at this pressure to allow
178 for microstructural equilibration. All measurements of water permeability were performed using the
179 steady-state flow method. Following microstructural equilibrium, a pressure gradient was imposed
180 across the sample and the flow rate measured using an electronic balance (with a precision ± 0.0005
181 g). Once steady-state flow had been established, the water permeability k_{water} was determined using
182 Darcy's relation:

183

184 $$\frac{Q}{A} = \frac{k_{water}}{\eta L}\left(P_{up} - P_{down}\right), \quad (1)$$

where Q is the volumetric flow rate, A is the cross-sectional area of the sample, P_{up} and P_{down} represent the upstream and downstream pressure, respectively (where P_{down} is the atmospheric pressure), L is the length of the sample, k_{water} is the permeability to water, and η is the viscosity of the pore fluid (taken here as 1.008×10^{-3} Pa.s). A pressure gradient (i.e. $P_{up} - P_{down}$) of 0.5 MPa was used for all of the steady-state measurements using water as the pore fluid (i.e. the mean pore fluid pressure, P_m, was 0.35 MPa, where $P_m = (P_{up} + P_{down})/2$).

Gas (argon) permeability was measured using either the steady-state method (for the andesites) or the pulse-decay method (for the basalt). The method chosen was based on the permeability of the sample: the steady-state method is better suited for high-permeability samples and the pulse-decay method is better suited for low-permeability samples (we note that there is no experimental bias between the methods: the permeability values of samples of intermediate permeability measured using both techniques in our laboratory are essentially identical). For the steady-state method, a pressure gradient was imposed across the sample (following microstructural equilibrium) and the outlet flow rate was measured using one of three Bronkhorst flowmeters. The choice of flowmeter depended on the permeability of the sample and therefore volumetric flow rate (the volumetric flow rate range for the three flowmeters: 1, 3, and 125 ml/min). Since the pore fluid is compressible, the raw permeability to gas k_{gas_raw} is expressed as [Scheidegger, 1947]:

$$\frac{Q}{A} = \frac{k_{gas\_raw}}{\eta L} \frac{(P_{up})^2 - (P_{down})^2}{2P_{down}}, \quad (2)$$

where η, the viscosity of the pore fluid, was taken as 2.21×10^{-5} Pa.s. Steady-state volumetric flow rate Q measurements were taken under several pore pressure gradients (i.e. $P_{up} - P_{down}$, where P_{down} is the atmospheric pressure) to check whether any auxiliary corrections were required. The

magnitude of pore pressure gradients used for the gas steady-state measurements varied depending on the permeability of the sample, but never exceeded 0.5 MPa (i.e. $P_m \leq 0.35$ MPa). We first plot $1/k_{gas\_raw}$ as a function of Q to check whether the Forchheimer correction is required. The correction is necessary if these data can be well described by a positive linear slope. The Forchheimer-corrected permeability is taken as the inverse of the *y*-intercept of the best-fit linear regression in the plot of $1/k_{gas\_raw}$ as a function of Q. An example of data that required the Forchheimer correction is shown in Figure 3a (for sample LAH4_7). If the Forchheimer correction is not required, we then check whether the Klinkenberg correction is required. To do so, we plot k_{gas_raw} as a function of the reciprocal mean pressure, $1/P_m$. The Klinkenberg correction is required if these data can be well described by a positive linear slope and, if true, the Klinkenberg-corrected permeability can be taken as the *y*-intercept of the best-fit linear regression in the plot of k_{gas_raw} as a function of $1/P_m$. The Forchheimer correction was required for the high-porosity andesites (Table 1) and the Klinkenberg correction was required for the low-porosity andesites (Table 1).

We used the pulse decay method [*Brace et al.*, 1968] to measure the gas permeability of the basalt sample. Following microstructural equilibrium at the target confining pressure, the decay of an initial pore pressure differential ($P_{up} - P_{down}$ = 0.5 MPa, where P_{down} is the atmospheric pressure; i.e. P_m = 0.35 MPa at the start of the experiment and decayed to the atmospheric pressure with time) was monitored using a pressure transducer following the closure of the upstream pressure inlet. The gas permeability k_{gas_raw} was then determined using the following relation:

$$k_{gas\_raw} = 2\frac{\eta L}{A}\frac{V_{up}}{{P_{up}}^2 - {P_{down}}^2}\frac{dP_{up}}{dt}, \quad (3)$$

where V_{up} is the volume of the upstream pore pressure circuit (= 7.8×10^{-6} m^3) and t is time. As before, we checked whether these data required any auxiliary corrections (the Forchheimer or Klinkenberg

correction). We found that the Klinkenberg correction was required for all of the basalt measurements (Table 1). An example of data that required the Klinkenberg correction is shown in Figure 3b (for sample EB_3).

Each permeability measurement was remeasured the following day. The sample was only removed, or subjected to the next confining pressure increment, if the retrieved permeability was the same as for the previous day. All the measurements in this study were performed under ambient laboratory temperatures.

3. Results

3.1 Connected porosity, specific surface area, and pore throat size distribution

The connected porosities of the andesite samples ranged from 0.08 to 0.27 and the connected porosities of the basalt samples were measured to be 0.04 (Table 1).

The specific surface area of the andesites varied from 15 to 100 $m^2 kg^{-1}$ (Table 1). We note that the specific surface area does not correlate with connected porosity: the andesite with the highest specific surface area (B5; Figure 1a) contains one of the lowest porosities (Table 1). The specific surface of the basalt block was measured to be 126 $m^2 kg^{-1}$ (Table 1).

Mercury porosimetry, which provides the pore throat size distribution, was performed on a low-porosity (B5) and a high-porosity (C8) andesite (Figure 4a) and the basalt (Figure 4b). About 50% of the porosity in andesite sample C8 (porosity = 0.144) is connected by pore throats with a radius ≥ 5 μm. Pore throats with a radius ≥ 5 μm connect only 35% of the porosity in andesite sample B5 (porosity = 0.076) (Figure 4a). Only 10% of the porosity in samples C8 and B5 is connected by pore throats with radii ≤ 0.5 μm (Figure 4a). The average pore throat radius was determined to be 2.15 and 1.05 μm for andesites C8 and B5, respectively. The mercury porosimetry data for the basalt show that 65% of the porosity is connected by pore throats with a radius below 0.5 μm (Figure 4b). The average pore throat radius for the basalt was determined to be 0.17 μm.

258

259 3.2 Influence of porosity on gas and water permeabilities

260 Gas and water permeabilities were measured for a suite of variably porous andesites from
261 Volcán de Colima (Figure 5; Table 1). These measurements were all collected under a constant
262 confining pressure of 2 MPa. First, and as observed in previous studies [e.g., *Farquharson et al*., 2015],
263 permeability is higher at higher porosities. Our data further show that gas permeability is higher than
264 water permeability over the entire porosity range (0.08 to 0.27) (Figure 5; Table 1). The difference
265 between gas and water permeability is between a factor of 1.1 and 5.5 (Figure 5; Table 1).

266

267 3.3 Influence of confining pressure on gas and water permeabilities

268 Gas and water permeabilities were measured on a sample of andesite (B5) and a sample of
269 basalt as a function of confining pressure (from 1 to 50 MPa) (Figure 6; Table 1). For both samples,
270 and both pore fluids, large decreases in permeability are observed between 1 and 10 MPa (Figure 6).
271 At confining pressures of 15 MPa and above, the permeability decrease per increment of confining
272 pressure is reduced (Figure 6). We also note that the absolute decrease in permeability from 1 to 50
273 MPa is much greater in the basalt than in the andesite: an order of magnitude in the case of the former
274 and only a factor of three for the latter (Figure 6; Table 1). The difference between gas and water
275 permeabilities is about a factor of three for the andesite and about a factor of four for the basalt (Table
276 1). For both rock types, this offset does not change significantly as confining pressure is increased
277 (Figure 6; Table 1).

278

279 **4. Discussion**

280 A difference in permeability when using different fluids is usually considered the
281 consequence of a physicochemical reaction between the mineral constituents of the rock and the pore
282 fluid, such as the reaction between liquid water and clay [*Faulkner and Rutter*, 2000, 2003; *Tanikawa*

283 *and Shimamoto* 2006; *Davy et al*., 2007; *Tanikawa and Shimamoto* 2009; *Behnsen and Faulkner*, 2011]
284 or the reaction between CO_2-enriched water and calcite [*Noiriel et al*., 2004; *Luquot and Gouze*, 2009].
285 It is for this reason that gas and water permeabilities are rarely measured and compared when the
286 rock-forming minerals are not expected to react with the pore fluid. One such study [*Brace et al*.,
287 1968] showed that gas and water permeabilities are essentially equal in intact Westerly granite
288 (porosity = 0.008) over a range of confining pressures between 10 and 100 MPa. Our new data show
289 that gas and water permeabilities can differ in volcanic rocks by up to a factor of five (Figures 5 and
290 6). Since these volcanic rocks do not contain minerals (such as clay) that are expected to undergo
291 significant physicochemical reactions in the presence of water, there must be another explanation
292 for the measured difference in gas and water permeability.
293 To better understand the microstructural path taken by the gas, we can use the Klinkenberg
294 slip factor, b, (which has the units of pressure) [*Klinkenberg*, 1941] to provide an estimate of the
295 average radius of the pores used by the gas molecules. The Klinkenberg slip factor has previously
296 been used to examine the average pore radius of the flow path in low-porosity rocks such as shales
297 [e.g., *Heller et al*., 2014; *Firouzi et al*., 2014; *Letham and Bustin*, 2015]. Since the mean free path is
298 inversely proportional to P_m, Poiseuille's law for gas flow in a cylindrical tube and Darcy's law for
299 flow in porous media yields the following relation:
300
301 $$k_{gas} = k_{gas\_raw}\left(1 + \frac{b}{P_m}\right), \quad (4)$$
302
303 where k_{gas} is the true (Klinkenberg-corrected) gas permeability. Therefore, and assuming tube-
304 shaped pores, the average pore radius r can be estimated using the following relation [*Civan*, 2010]:
305
306 $$r = \frac{4}{b}\eta\sqrt{\frac{\pi R_g T}{2M_w}}, \quad (5)$$

where R_g is the ideal gas constant (taken as 8.31 J mol^{-1} K^{-1}), T is the temperature (taken as 293 K), and M_w is the molecular mass of the pore fluid (taken as 0.03995 kg mol^{-1}). The average pore radius that controls the flow of gas molecules (calculated using Equation (5)) for the sample of andesite (B5) and basalt as a function of confining pressure is shown in Figure 7. The calculations show that the average pore radius in the andesite is ~0.5 μm at low pressure (between 1 and 2 MPa) and evolves to, and stays constant at, ~0.2-0.25 μm when the confining pressure is at or above 15 MPa (Figure 7; Table 1). The average pore radius in the basalt is ~0.3 μm at a confining pressure of 1 MPa (Figure 7; Table 1). The average pore radius in the basalt reduces to, and stays constant at, ~0.13-0.16 μm when the confining pressure is at or above 15 MPa (Figure 7; Table 1). The Klinkenberg slip factor can also be used to estimate the width of "slit-shaped" pores (i.e. microcracks) [e.g., *Heller et al*., 2014; *Letham and Bustin*, 2015], which, according to our microstructural analyses (Figures 1 and 2) and mercury injection data (Figure 4), may better suit these rocks, especially the basalt (Figures 2 and 4b). However, the widths predicted using the equation presented in *Heller et al*. [2014] and *Letham and Bustin* [2015] are within the range ~3-11.5 and ~3-6.5 μm for the andesite and basalt, respectively. We consider such widths unrealistically high. The basalt, for example, not only has an average pore throat diameter of 0.34 μm (determined by mercury porosimetry), but the mercury injection data also show that only ~2% of the void space is connected by pore throats with diameters larger than 6.5 μm (Figure 4b). Although it is difficult at present to forward a reason as to why the average width of a slit-shaped pore provides an overestimation of the size of the microstructural elements carrying the gas, while the average radius of a tube-shaped pore does not, we highlight that these geometries only represent end-member geometries in rocks characterised by geometrically complex pore networks (Figures 1, 2, and 4). As a result, although the average pore radii provided in Figure 7 inform on the size of the microstructural element used by the gas molecules (i.e. submicron), we highlight that these values are estimations that assume a cylindrical pore shape. The average pore

radius used by the gas molecules in the basalt predicted using Equation 5 (~0.13-0.3 μm; Figure 7) is very similar to the average pore throat radius determined by the mercury porosimetry (0.17 μm). This is likely a consequence of the relatively narrow range of pore and pore throat sizes (Figure 4b) within the basalt: 80% of the void space is connected by pore throat radii between ~0.7 and ~1.5 μm (Figure 4b). However, the average pore throat radius determined by mercury porosimetry is 2.15 and 1.05 μm for andesites C8 and B5, respectively, much greater than the radii predicted using the Klinkenberg slip factor (~0.25-0.5 μm; Figure 7). Although the andesites contain microstructural elements (microcracks and tubes) of varying diameter (Figure 4a), resulting in a high average pore throat radius, pores within this size range are likely not used for flow, which is likely obliged to negotiate through narrow microstructural elements (on the submicron scale).

Based on the mercury porosimetry (Figure 4) and the average pore radii (assuming a cylindrical pore shape) predicted using Equation 5 (Figure 7), it is likely that the gas in both samples (andesite and basalt) is travelling through thin and tortuous/rough microcracks. This inference is supported by the evolution of permeability as confining pressure increases (Figure 6). A reduction in the permeability of microcracked volcanic rocks with increasing confining pressure has been previously explained by the narrowing of microcrack apertures or the closing of microcracks [e.g., *Vinciguerra et al*., 2005; *Nara et al.*, 2011; *Fortin et al.*, 2011; *Heap et al.*, 2017], supported here by the decrease in our average pore radii estimations with increasing confining pressure (Figure 7). However, the reduction in permeability with confining pressure for the volcanic rocks studied herein (Figure 6) are much less than those typically observed for microcracked granites [e.g., *Le Ravalec et al*., 1996; *David et al*., 1999; *Darot and Reuschlé*, 2000]. We consider this a consequence of the tortuous/rough nature of the microcracks within the studied andesite and basalt (Figures 1 and 2): tortuous and rough cracks require higher pressures to close than straight and smooth cracks [e.g., *Pérez-Flores et al*., 2017]. Further, the more significant decrease in the permeability of the basalt with increasing confining pressure—one order of magnitude compared to a factor of three in the andesite

357 (Figure 6)—must require that the microcracks supporting fluid flow in the andesite are more difficult
358 to close than those in the basalt. Indeed, qualitative microstructural observations suggest that the
359 microcracks in the andesite are shorter and more tortuous/kinked than those in the basalt (Figures
360 1 and 2), adding confidence to this hypothesis.

361 The estimations of average pore radii shown in Figure 7, and the average pore throat radii
362 determined from the mercury porosimetry data, highlight the microstructural complexity of volcanic
363 rocks. To emphasise, although ~90% of the void volume in the andesite is connected by pore throats
364 greater than 1 μm (Figure 4a), our pore radii predictions (Figure 7) suggest the gas flow is controlled
365 by microstructural elements that have an average radius of ~0.2-0.25 μm. To the authors' knowledge,
366 this represents the first time the Klinkenberg slip factor has been used to estimate the average pore
367 radius of gas flow paths in volcanic materials; we recommend that this method is utilised in future
368 studies.

369 We must now consider why these thin microstructural elements could be inaccessible to
370 water. *Faulkner and Rutter* [2000] inferred that the lower permeability to water than to gas in clay-
371 bearing fault gouge was a result of layers of structured water adsorbed onto the phyllosilicate
372 mineral surfaces, thereby reducing the effective pore throat aperture and reducing permeability.
373 However, there are no clay minerals in our studied materials. The permeability experiments of
374 *Klinkenberg* [1941], although designed to test the hypothesis that adsorbed molecules on the walls
375 of small capillaries in porous materials could inhibit fluid flow, found that the permeabilities to
376 different liquids were within experimental error. However, as discussed in *Faulkner and Rutter*
377 [2000], any water adsorption effect in the high-permeability (~10^{-14} m^2) glass filters of *Klinkenberg*
378 [1941] was likely masked by their large pore throat apertures. In other words, perhaps the pore radii
379 of the volcanic rocks tested herein are sufficiently narrow to observe a difference due to water
380 adsorption, while the apertures of glass filters tested by *Klinkenberg* [1941] are not. Although we
381 cannot advance a definitive reason for the difference between gas and water permeability in the

382 volcanic rocks measured herein, we speculate that water molecules adsorbed onto the surface of the
383 thin (~0.1-0.5 μm) microstructural elements are capable of narrowing their aperture or rendering
384 them inaccessible to the flow of water. It is the complex nature and poor connectivity of the void
385 space in these volcanic rocks (Figures 1, 2, and 4) that obliges fluid to negotiate these thin
386 microstructural elements, which are also characterised by complex geometries (i.e. tortuous, kinked,
387 and rough; see discussion above). We further speculate that it is the tortuous, kinked, and rough
388 nature of the microcracks that allows the adsorption of water to reduce the water permeability.
389 Absorbed water molecules need not obstruct the entire length of a microcrack, but only a small
390 section – perhaps a particularly rough-walled section or at a tight bend or kink. Although this complex
391 microstructure is typical of lavas [e.g., *Colombier et al.*, 2017], it is unclear at present whether volcanic
392 rocks that contain a permeable backbone of large, well-connected tubes—such as some pumices—
393 will also display differences between gas and water permeabilities.

394 The implication of these data is that the permeability of the rocks comprising a volcanic
395 edifice will be higher to gas (e.g., CO_2 and SO_2; *Edmonds et al*. [2003]) than to liquid (e.g., the
396 infiltration of meteoric and seawater and the circulation of groundwater/hydrothermal fluids;
397 *Hurwitz et al*., [2003]). Further, permeability may vary in zones that experience fluctuations in pore
398 fluid state as a result of fluctuating temperature or pressure. For example, a reduction in temperature
399 that results in a change in fluid state from gas to liquid may promote pore pressure build-up as a
400 result of a decrease in permeability. Alternatively, unloading of the edifice (due to mass movement
401 events, for example) could trigger decompression of the interstitial pore fluid, prompting a phase
402 change in the opposite direction (i.e. liquid to vapour). Importantly, the saturation curve for water
403 (which delineates the pressure-temperature boundary between liquid and vapour) occurs within
404 conditions relevant for a shallow edifice. Indeed, electrical resistivity tomography of the shallow
405 hydrothermal system of Campi Flegrei (Italy) shows a complex configuration of gaseous and liquid
406 zones, and zones characterised by mixtures of gases and liquids [*Byrdina et al.*, 2014]. The data

407 presented herein therefore have important ramifications for the distribution and build-up of pore
408 pressure in a volcanic system. Further, the choice of pore fluid used in laboratory investigations and
409 the choice of permeability values to be used in fluid flow modelling should be carefully considered
410 [e.g., *Collombet*, 2009; *Collinson and Neuberg*, 2012; *Fournier and Chardot*, 2012; *Chevalier et al.*,
411 2017]. Finally, we also highlight that care should be taken when collating porosity-permeability data
412 from published studies.
413
414 **5. Conclusions**
415 Our laboratory measurements highlight that gas permeability can be a factor of two to five
416 higher than water permeability in volcanic rocks. Using the Klinkenberg slip factor (assuming tube-
417 shaped pores), we estimate the average radius of the microstructural elements used by the gas flow
418 to be ~0.1-0.5 μm. Although we cannot definitively advance a reason for the difference in gas and
419 water permeability, we speculate that water adsorption on the surfaces of these thin microstructural
420 elements—assumed here to be microcracks—may reduce their effective radius and/or prevent
421 access, thus reducing the water permeability of these volcanic rocks. We further speculate that it is
422 the tortuous, kinked, and rough nature of the microcracks that allows the adsorption of water to
423 reduce the water permeability. Absorbed water molecules need not obstruct the entire length of a
424 microcrack, but only a small section – perhaps a particularly rough-walled section or at a tight bend
425 or kink. Our data highlight the need for further studies that explore differences between gas and
426 water permeabilities in a range of volcanic materials. A difference between gas and water
427 permeabilities in volcanic materials has important ramifications for the distribution and build-up of
428 pore pressure in hydrothermal and geothermal systems in volcanically active regions, as well as
429 volcanic systems themselves.
430
431 **Acknowledgements**

M.J. Heap acknowledges an Initiative d'Excellence (IDEX) "Attractivité" grant (VOLPERM) and P. Baud and J.I. Farquharson acknowledge an IDEX "Contrats doctoraux" grant, both funded by the University of Strasbourg. Gilles Morvan is thanked for his assistance using the SEM. We would like to thank S. Mueller, O. Spieler, and N. Varley for their role in collecting the andesites from Volcán de Colima in 2004 (field campaign supported by the R&D Programme GEOTECHNOLOGIEN, funded by the German Ministry of Education and Research (BMBF), and German Research Foundation (DFG) grant PTJ MGS/03G584A-SUNDAARC-DEVACOM). We thank P.G. Meredith for providing the samples of basalt from Mt Etna. The mercury porosimetry was performed at the University of Aberdeen; thanks go to Dave Healy for providing the final measurement free of charge. We thank two anonymous reviewers and the editor (Kelly Russell) for comments that helped improve this manuscript.

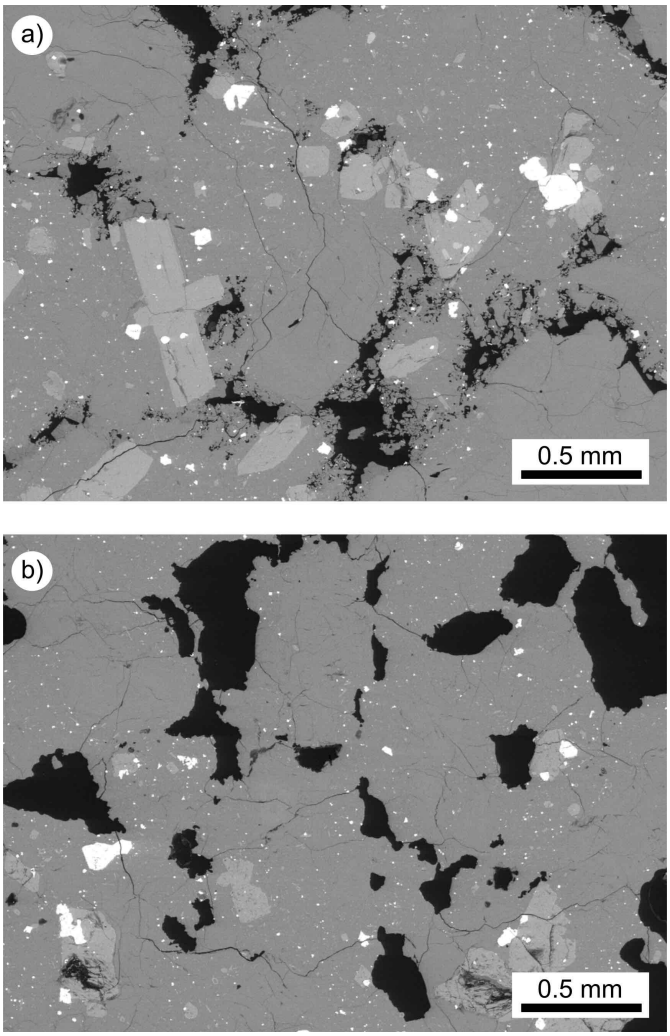

444

445 **Figure 1**. (a) Backscattered scanning electron microscope image of andesite sample B5 (from Volcán
446 de Colima, Mexico). (b) Backscattered scanning electron microscope image of andesite sample C8
447 (from Volcán de Colima). Both samples are characterised by a complex microstructure containing
448 both pores and microcracks (see text for details).

449

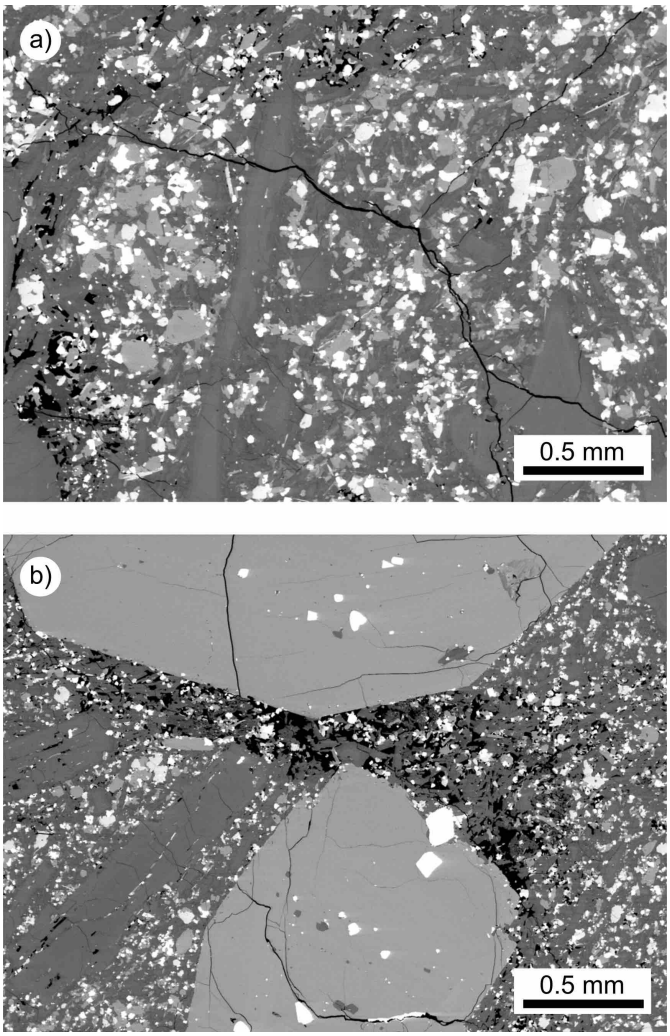

450

451 **Figure 2**. (a) Backscattered scanning electron microscope image of the basalt from Mt Etna (Italy)
452 showing a long microcrack that traverses the crystallised groundmass. (b) Backscattered scanning
453 electron microscope image of the basalt from Mt Etna showing a pocket of micropores sandwiched
454 between two phenocrysts (see text for details).

455

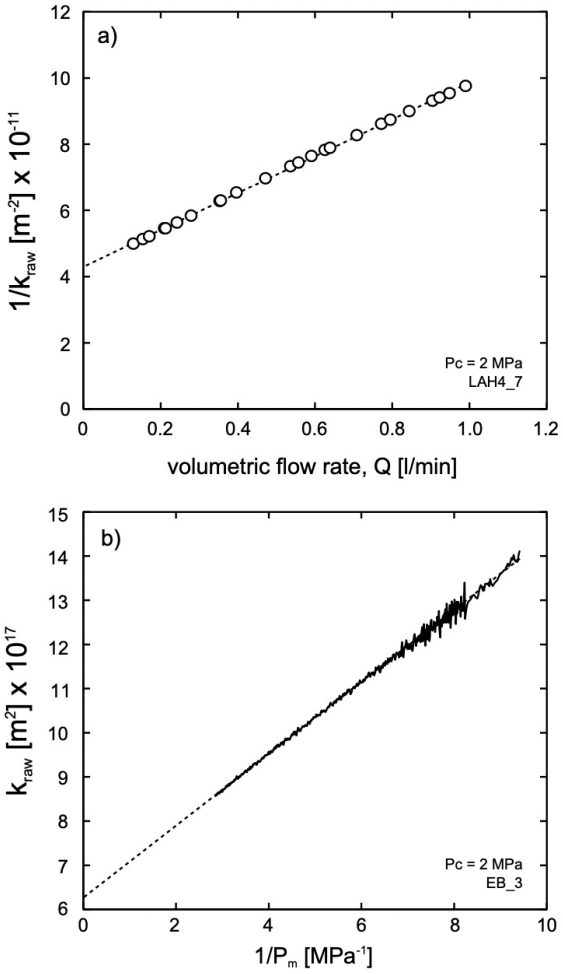

Figure 3. (a) Data that require a Forchheimer correction. The graph is a plot of $1/k_{gas\_raw}$ as a function of volumetric flow rate, Q. The Forchheimer correction is necessary if the data can be well described by a positive linear slope. The Forchheimer-corrected permeability is taken as the inverse of the y-intercept of the best-fit linear regression. In the example shown here, the permeability is 2.33 × 10^{-12} m^2 (Table 1). (b) Data that require a Klinkenberg correction. The graph is a plot of k_{gas_raw} as a function of the reciprocal mean pressure $1/P_m$, where P_m is the mean pore fluid pressure (i.e. $(P_{up} + P_{down})/2$). The Klinkenberg correction is required if the data can be well described by a positive linear slope and, if true, the Klinkenberg-corrected permeability is taken as the y-intercept of the best-fit linear regression. In the example shown here, the permeability is 6.29 × 10^{-17} m^2 (Table 1).

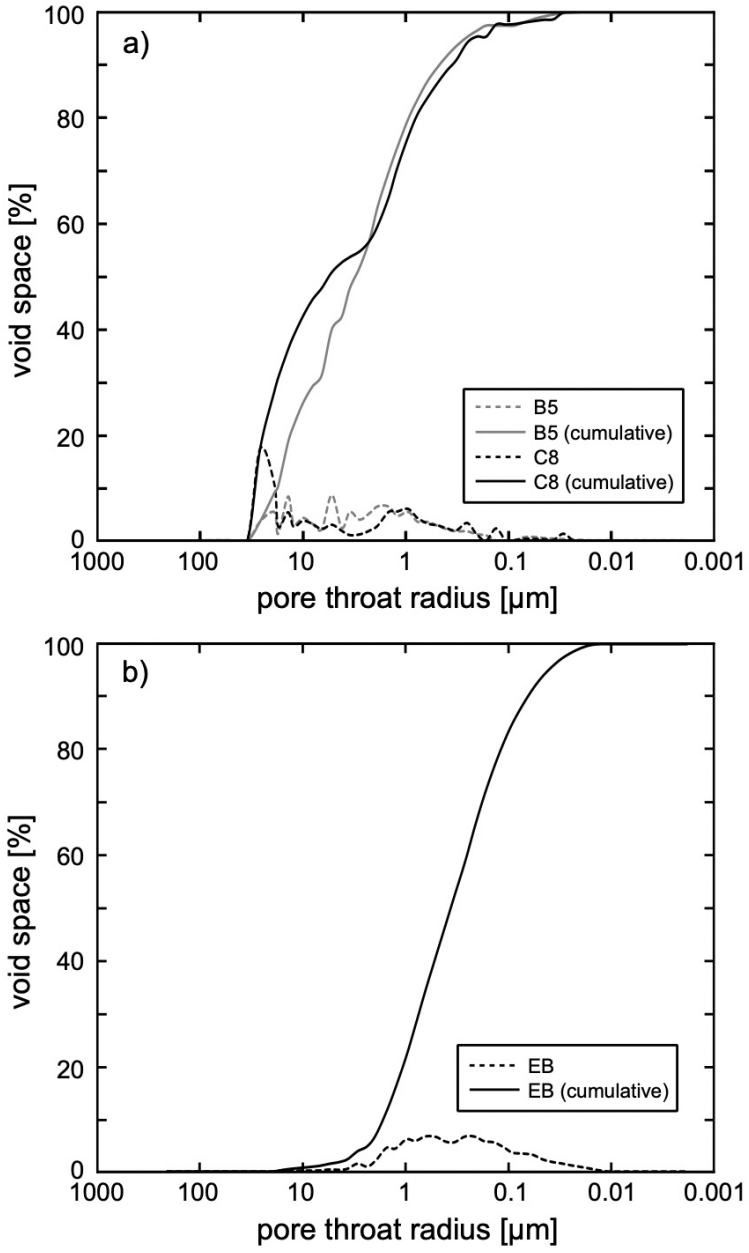

466

467 **Figure 4**. (a) Pore throat radius distributions, determined by mercury injection, for andesite samples
468 B5 and C8 (from Volcán de Colima, Mexico). (b) Pore throat radius distribution, determined by
469 mercury injection, for the basalt from Mt Etna (Italy). Dashed curves show the void space and the
470 solid curves show the cumulative void space. The mercury injection data was corrected for the "low
471 pressure correction" recommended by ASTM International [ASTM D4404-10].

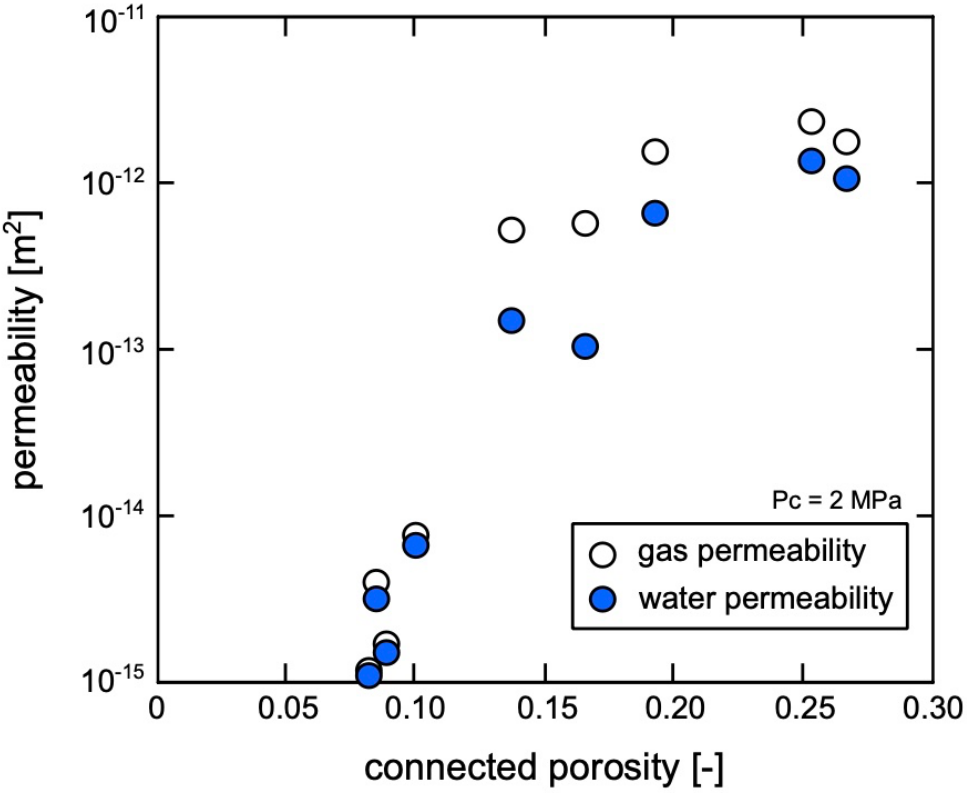

472

473 **Figure 5**. Gas (white circles) and water (blue circles) permeability as a function of connected porosity
474 for a suite of andesites from Volcán de Colima (Mexico). All measurements were performed under a
475 confining pressure of 2 MPa. Error due to transducer precision is smaller than the symbol size. Data
476 available in Table 1.

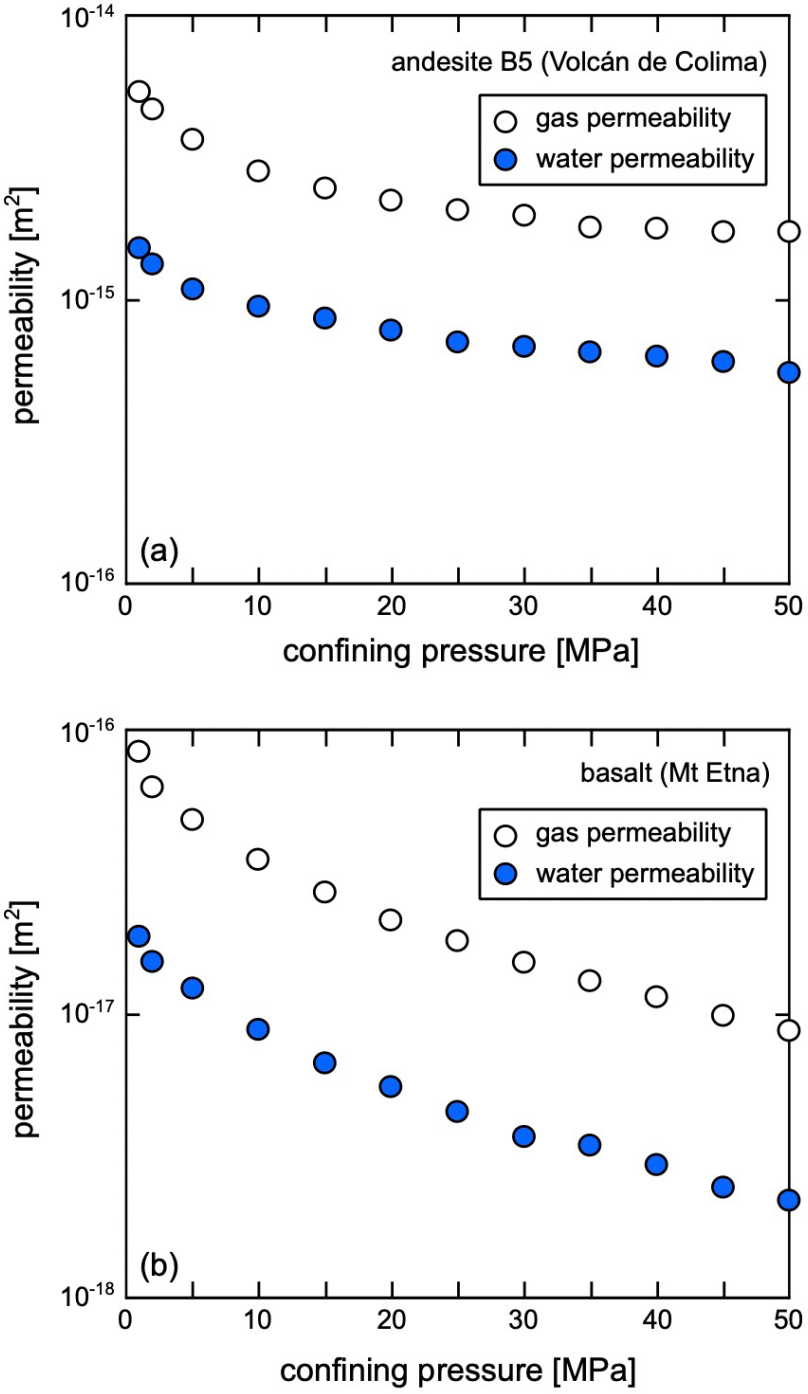

477

478 **Figure 6**. Gas (white circles) and water (blue circles) permeability as a function of confining pressure
479 (from 1 to 50 MPa) for (a) andesite sample B5 (from Volcán de Colima, Mexico) and (b) the basalt
480 from Mt Etna (Italy). Error due to transducer precision is smaller than the symbol size. Data available
481 in Table 1.

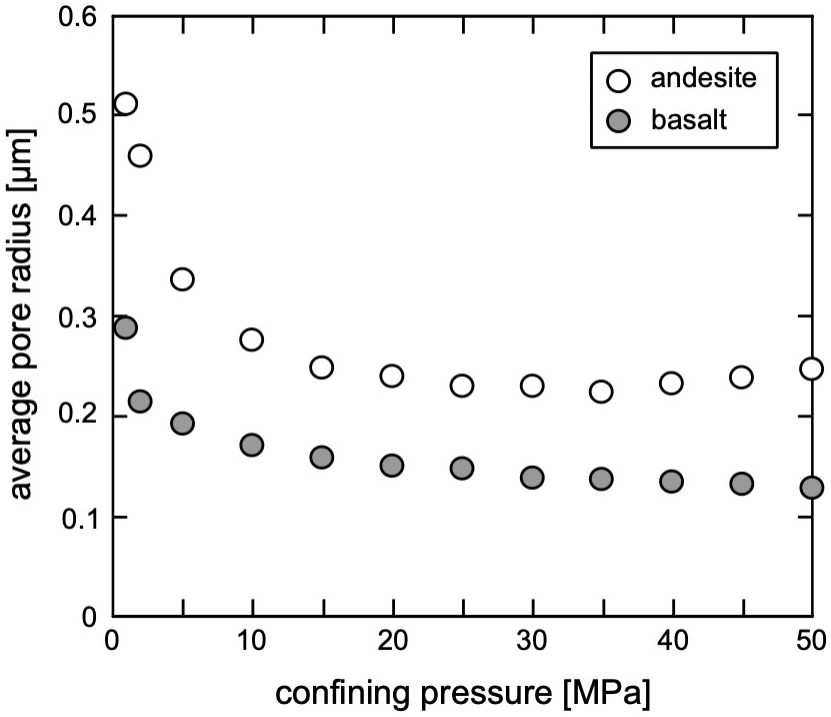

482

483 **Figure 7**. Average pore radius for andesite sample B5 (from Volcán de Colima, Mexico) (white circles)
484 and the basalt from Mt Etna (Italy) (grey circles) as a function of confining pressure (from 1 to 50
485 MPa), as calculated using the Klinkenberg slip factor (see Equation 5 and text for details). Data
486 available in Table 1.

487

References

Allard, P., Behncke, B., D'Amico, S., Neri, M., & Gambino, S. (2006). Mount Etna 1993–2005: anatomy of an evolving eruptive cycle. *Earth-Science Reviews*, *78*(1-2), 85-114.

ASTM D4404-10, Standard Test Method for Determination of Pore Volume and Pore Volume Distribution of Soil and Rock by Mercury Intrusion Porosimetry, ASTM International, West Conshohocken, PA, 2010, www.astm.org.

Barberi, F., Bertagnini, A., Landi, P., & Principe, C. (1992). A review on phreatic eruptions and their precursors. *Journal of Volcanology and Geothermal Research*, *52*(4), 231-246.

Behnsen, J., & Faulkner, D. R. (2011). Water and argon permeability of phyllosilicate powders under medium to high pressure. *Journal of Geophysical Research: Solid Earth*, *116*(B12).

Blower, J. (2001). Factors controlling permeability-porosity relationships in magma. *Bulletin of Volcanology*, *63*(7), 497-504.

Brace, W., Walsh, J. B., & Frangos, W. T. (1968). Permeability of granite under high pressure. *Journal of Geophysical research*, *73*(6), 2225-2236.

Brunauer, S., Emmett, P. H., & Teller, E. (1938). Adsorption of gases in multimolecular layers. *Journal of the American Chemical Society*, *60*(2), 309-319.

Burgisser, A., Chevalier, L., Gardner, J. E., & Castro, J. M. (2017). The percolation threshold and permeability evolution of ascending magmas. *Earth and Planetary Science Letters*, *470*, 37-47.

Byrdina, S., Vandemeulebrouck, J., Cardellini, C., Legaz, A., Camerlynck, C., Chiodini, G., ... & Carrier, A. (2014). Relations between electrical resistivity, carbon dioxide flux, and self-potential in the shallow hydrothermal system of Solfatara (Phlegrean Fields, Italy). *Journal of Volcanology and Geothermal Research*, *283*, 172-182.

Civan, F. (2010). Effective correlation of apparent gas permeability in tight porous media. *Transport in porous media*, *82*(2), 375-384.

Chevalier, L., Collombet, M., & Pinel, V. (2017). Temporal evolution of magma flow and degassing conditions during dome growth, insights from 2D numerical modeling. *Journal of Volcanology and Geothermal Research*, *333*, 116-133.

Chiodini, G., Allard, P., Caliro, S., & Parello, F. (2000). ^{18}O exchange between steam and carbon dioxide in volcanic and hydrothermal gases: implications for the source of water. *Geochimica et Cosmochimica Acta*, *64*(14), 2479-2488.

Collinson, A. S. D., & Neuberg, J. W. (2012). Gas storage, transport and pressure changes in an evolving permeable volcanic edifice. *Journal of Volcanology and Geothermal Research*, *243*, 1-13.

Collombet, M. (2009). Two-dimensional gas loss for silicic magma flows: toward more realistic numerical models. *Geophysical Journal International*, *177*(1), 309-318.

Colombier, M., Wadsworth, F. B., Gurioli, L., Scheu, B., Kueppers, U., Di Muro, A., & Dingwell, D. B. (2017). The evolution of pore connectivity in volcanic rocks. *Earth and Planetary Science Letters*, *462*, 99-109.

Costa, A. (2006). Permeability-porosity relationship: A reexamination of the Kozeny-Carman equation based on a fractal pore-space geometry assumption. *Geophysical Research Letters*, *33*(2).

Darcy, H. (1856). The public fountains of the city of Dijon. *Dalmont, Paris*, *647*.

Darot, M., & Reuschlé, T. (2000). Acoustic wave velocity and permeability evolution during pressure cycles on a thermally cracked granite. *International Journal of Rock Mechanics and Mining Sciences*, *37*(7), 1019-1026.

David, C., Menéndez, B., & Darot, M. (1999). Influence of stress-induced and thermal cracking on physical properties and microstructure of La Peyratte granite. *International Journal of Rock Mechanics and Mining Sciences*, *36*(4), 433-448.

Davy, C. A., Skoczylas, F., Barnichon, J. D., & Lebon, P. (2007). Permeability of macro-cracked argillite under confinement: gas and water testing. *Physics and Chemistry of the Earth, Parts A/B/C*, *32*(8), 667-680.

Degruyter, W., Burgisser, A., Bachmann, O., & Malaspinas, O. (2010). Synchrotron X-ray microtomography and lattice Boltzmann simulations of gas flow through volcanic pumices. *Geosphere*, *6*(5), 470-481.

Edmonds, M., Oppenheimer, C., Pyle, D. M., Herd, R. A., & Thompson, G. (2003). SO 2 emissions from Soufrière Hills Volcano and their relationship to conduit permeability, hydrothermal interaction and degassing regime. *Journal of Volcanology and Geothermal Research*, *124*(1), 23-43.

Eichelberger, J. C., Carrigan, C. R., Westrich, H. R., & Price, R. H. (1986). Non-explosive silicic volcanism. *Nature*, *323*(6089), 598-602.

Farquharson, J., Heap, M. J., Varley, N. R., Baud, P., & Reuschlé, T. (2015). Permeability and porosity relationships of edifice-forming andesites: a combined field and laboratory study. *Journal of Volcanology and Geothermal Research*, *297*, 52-68.

Farquharson, J. I., Heap, M. J., Lavallée, Y., Varley, N. R., & Baud, P. (2016). Evidence for the development of permeability anisotropy in lava domes and volcanic conduits. *Journal of Volcanology and Geothermal Research*, *323*, 163-185.

Farquharson, J. I., Wadsworth, F. B., Heap, M. J., & Baud, P. (2017). Time-dependent permeability evolution in compacting volcanic fracture systems and implications for gas overpressure. *Journal of Volcanology and Geothermal Research*, *339*, 81-97.

Faulkner, D. R., & Rutter, E. H. (2000). Comparisons of water and argon permeability in natural clay-bearing fault gouge under high pressure at 20° C. *Journal of Geophysical Research: Solid Earth*, *105*(B7), 16415-16426.

Faulkner, D. R., & Rutter, E. H. (2003). The effect of temperature, the nature of the pore fluid, and subyield differential stress on the permeability of phyllosilicate-rich fault gouge. *Journal of Geophysical Research: Solid Earth*, *108*(B5).

Firouzi, M., Alnoaimi, K., Kovscek, A., & Wilcox, J. (2014). Klinkenberg effect on predicting and measuring helium permeability in gas shales. *International Journal of Coal Geology*, *123*, 62-68.

Forchheimer, P. H. (1901). Wasserbewegung durch boden. *Zeitz. Ver. Duetch Ing.*, *45*, 1782-1788.

Fortin, J., Stanchits, S., Vinciguerra, S., & Guéguen, Y. (2011). Influence of thermal and mechanical cracks on permeability and elastic wave velocities in a basalt from Mt. Etna volcano subjected to elevated pressure. *Tectonophysics*, *503*(1), 60-74.

Fournier, N., & Chardot, L. (2012). Understanding volcano hydrothermal unrest from geodetic observations: Insights from numerical modeling and application to White Island volcano, New Zealand. *Journal of Geophysical Research: Solid Earth*, *117*(B11).

Gaunt, H. E., Sammonds, P. R., Meredith, P. G., Smith, R., & Pallister, J. S. (2014). Pathways for degassing during the lava dome eruption of Mount St. Helens 2004–2008. *Geology*, *42*(11), 947-950.

Giggenbach, W. F., & Soto, R. C. (1992). Isotopic and chemical composition of water and steam discharges from volcanic-magmatic-hydrothermal systems of the Guanacaste Geothermal Province, Costa Rica. *Applied geochemistry*, *7*(4), 309-332.

Guéguen, Y., & Palciauskas, V. (1994). *Introduction to the physics of rocks*. Princeton University Press.

Heap, M. J., Baud, P., Meredith, P. G., Vinciguerra, S., Bell, A. F., & Main, I. G. (2011). Brittle creep in basalt and its application to time-dependent volcano deformation. *Earth and Planetary Science Letters*, *307*(1), 71-82.

Heap, M. J., Lavallée, Y., Petrakova, L., Baud, P., Reuschlé, T., Varley, N. R., & Dingwell, D. B. (2014a). Microstructural controls on the physical and mechanical properties of edifice-forming andesites at Volcán de Colima, Mexico. *Journal of Geophysical Research: Solid Earth*, *119*(4), 2925-2963.

585 Heap, M. J., Baud, P., Meredith, P. G., Vinciguerra, S., & Reuschlé, T. (2014b). The permeability and
586 elastic moduli of tuff from Campi Flegrei, Italy: implications for ground deformation
587 modelling. *Solid Earth*, *5*(1), 25.
588 Heap, M. J., Farquharson, J. I., Baud, P., Lavallée, Y., & Reuschlé, T. (2015). Fracture and compaction of
589 andesite in a volcanic edifice. *Bulletin of Volcanology*, *77*(6), 55.
590 Heap, M. J., & Kennedy, B. M. (2016). Exploring the scale-dependent permeability of fractured
591 andesite. *Earth and Planetary Science Letters*, *447*, 139-150.
592 Heap, M. J., Russell, J. K., & Kennedy, L. A. (2016). Mechanical behaviour of dacite from Mount St.
593 Helens (USA): A link between porosity and lava dome extrusion mechanism (dome or spine)?
594 *Journal of Volcanology and Geothermal Research*, *328*, 159-177.
595 Heap, M. J., Kennedy, B. M., Farquharson, J. I., Ashworth, J., Mayer, K., Letham-Brake, M., ... & Siratovich,
596 P. (2017). A multidisciplinary approach to quantify the permeability of the Whakaari/White
597 Island volcanic hydrothermal system (Taupo Volcanic Zone, New Zealand). *Journal of*
598 *Volcanology and Geothermal Research*, *332*, 88-108.
599 Heller, R., Vermylen, J., & Zoback, M. (2014). Experimental investigation of matrix permeability of gas
600 shales. *AAPG Bulletin*, *98*(5), 975-995.
601 Houghton, B. F., & Nairn, I. A. (1991). The 1976–1982 Strombolian and phreatomagmatic eruptions
602 of White Island, New Zealand: eruptive and depositional mechanisms at a 'wet' volcano.
603 *Bulletin of Volcanology*, *54*(1), 25-49.
604 Hurwitz, S., Kipp, K. L., Ingebritsen, S. E., & Reid, M. E. (2003). Groundwater flow, heat transport, and
605 water table position within volcanic edifices: Implications for volcanic processes in the Cascade
606 Range. *Journal of Geophysical Research: Solid Earth*, *108*(B12).
607 Klinkenberg, L. J. (1941). The permeability of porous media to liquids and gases. In *Drilling and*
608 *production practice*. American Petroleum Institute.
609 Kendrick, J. E., Lavallée, Y., Hess, K. U., Heap, M. J., Gaunt, H. E., Meredith, P. G., & Dingwell, D. B. (2013).
610 Tracking the permeable porous network during strain-dependent magmatic flow. *Journal of*
611 *Volcanology and Geothermal Research*, *260*, 117-126.
612 Kolzenburg, S., Heap, M. J., Lavallée, Y., Russell, J. K., Meredith, P. G., & Dingwell, D. B. (2012). Strength
613 and permeability recovery of tuffisite-bearing andesite. *Solid Earth*, *3*(2), 191.
614 Kushnir, A. R., Martel, C., Bourdier, J. L., Heap, M. J., Reuschlé, T., Erdmann, S., ... & Cholik, N. (2016).
615 Probing permeability and microstructure: Unravelling the role of a low-permeability dome on
616 the explosivity of Merapi (Indonesia). *Journal of Volcanology and Geothermal Research*, *316*, 56-
617 71.
618 Kushnir, A. R., Martel, C., Champallier, R., & Arbaret, L. (2017a). In situ confirmation of permeability
619 development in shearing bubble-bearing melts and implications for volcanic outgassing. *Earth*
620 *and Planetary Science Letters*, *458*, 315-326.
621 Kushnir, A. R. L., Martel, C., Champallier, R., & Wadsworth, F. B. (2017b). Permeability evolution in
622 variably glassy basaltic andesites measured under magmatic conditions. *Geophysical Research*
623 *Letters*, DOI: 10.1002/2017GL074042.
624 Le Ravalec, M., Darot, M., Reuschlé, T., & Guéguen, Y. (1996). Transport properties and
625 microstructural characteristics of a thermally cracked mylonite. *Pure and Applied Geophysics*,
626 *146*(2), 207-227.
627 Letham, E. A., & Bustin, R. M. (2016). Klinkenberg gas slippage measurements as a means for shale
628 pore structure characterization. *Geofluids*, *16*(2), 264-278.
629 Lavallée, Y., Benson, P. M., Heap, M. J., Hess, K. U., Flaws, A., Schillinger, B., ... & Dingwell, D. B. (2013).
630 Reconstructing magma failure and the degassing network of dome-building eruptions. *Geology*,
631 *41*(4), 515-518.
632 Lindoo, A., Larsen, J. F., Cashman, K. V., Dunn, A. L., & Neill, O. K. (2016). An experimental study of
633 permeability development as a function of crystal-free melt viscosity. *Earth and Planetary*
634 *Science Letters*, *435*, 45-54.

635 Luquot, L., & Gouze, P. (2009). Experimental determination of porosity and permeability changes
636 induced by injection of CO_2 into carbonate rocks. *Chemical Geology*, *265*(1), 148-159.
637 Mayer, K., Scheu, B., Gilg, H. A., Heap, M. J., Kennedy, B. M., Lavallée, Y., ... & Dingwell, D. B. (2015).
638 Experimental constraints on phreatic eruption processes at Whakaari (White Island volcano).
639 *Journal of Volcanology and Geothermal Research*, *302*, 150-162.
640 Melnik, O., Barmin, A. A., & Sparks, R. S. J. (2005). Dynamics of magma flow inside volcanic conduits
641 with bubble overpressure buildup and gas loss through permeable magma. *Journal of*
642 *Volcanology and Geothermal Research*, *143*(1), 53-68.
643 Montanaro, C., Scheu, B., Mayer, K., Orsi, G., Moretti, R., Isaia, R., & Dingwell, D. B. (2016). Experimental
644 investigations on the explosivity of steam-driven eruptions: A case study of Solfatara volcano
645 (Campi Flegrei). *Journal of Geophysical Research: Solid Earth*, *121*(11), 7996-8014.
646 Mueller, S., Melnik, O., Spieler, O., Scheu, B., & Dingwell, D. B. (2005). Permeability and degassing of
647 dome lavas undergoing rapid decompression: an experimental determination. *Bulletin of*
648 *Volcanology*, *67*(6), 526-538.
649 Mueller, S., Scheu, B., Spieler, O., & Dingwell, D. B. (2008). Permeability control on magma
650 fragmentation. *Geology*, *36*(5), 399-402.
651 Nara, Y., Meredith, P. G., Yoneda, T., & Kaneko, K. (2011). Influence of macro-fractures and micro-
652 fractures on permeability and elastic wave velocities in basalt at elevated
653 pressure. *Tectonophysics*, *503*(1), 52-59.
654 Noiriel, C., Gouze, P., & Bernard, D. (2004). Investigation of porosity and permeability effects from
655 microstructure changes during limestone dissolution. *Geophysical Research Letters*, *31*(24).
656 Pérez-Flores, P., Wang, G., Mitchell, T. M., Meredith, P. G., Nara, Y., Sarkar, V., & Cembrano, J. (2017).
657 The effect of offset on fracture permeability of rocks from the Southern Andes Volcanic Zone,
658 Chile. *Journal of Structural Geology*, *104*, 142-158.
659 Reid, M. E. (2004). Massive collapse of volcano edifices triggered by hydrothermal
660 pressurization. *Geology*, *32*(5), 373-376.
661 Rust, A. C., & Cashman, K. V. (2004). Permeability of vesicular silicic magma: inertial and hysteresis
662 effects. *Earth and Planetary Science Letters*, *228*(1), 93-107.
663 Saar, M. O., & Manga, M. (1999). Permeability-porosity relationship in vesicular basalts. *Geophysical*
664 *Research Letters*, *26*(1), 111-114.
665 Sparks, R. S. J. (1997). Causes and consequences of pressurisation in lava dome eruptions. *Earth and*
666 *Planetary Science Letters*, *150*(3-4), 177-189.
667 Stanchits, S., Vinciguerra, S., & Dresen, G. (2006). Ultrasonic velocities, acoustic emission
668 characteristics and crack damage of basalt and granite. *Pure and Applied Geophysics*, *163*(5-6),
669 975-994.
670 Tanikawa, W., & Shimamoto, T. (2006). Klinkenberg effect for gas permeability and its comparison to
671 water permeability for porous sedimentary rocks. *Hydrology and Earth System Sciences*
672 *Discussions*, *3*(4), 1315-1338.
673 Tanikawa, W., & Shimamoto, T. (2009). Comparison of Klinkenberg-corrected gas permeability and
674 water permeability in sedimentary rocks. *International Journal of Rock Mechanics and Mining*
675 *Sciences*, *46*(2), 229-238.
676 Taran, Y., Fischer, T. P., Pokrovsky, B., Sano, Y., Armienta, M. A., & Macias, J. L. (1998). Geochemistry
677 of the volcano-hydrothermal system of El Chichón Volcano, Chiapas, Mexico. *Bulletin of*
678 *Volcanology*, *59*(6), 436-449.
679 Varley, N., & Komorowski, J.-C. (2018). Volcán de Colima: Managing the Threat. Springer-Verlag
680 Berlin Heidelberg. ISBN 978-3-642-25910-4.
681 Vasseur, J., & Wadsworth, F. B. (2017). Sphere models for pore geometry and fluid permeability in
682 heterogeneous magmas. *Bulletin of Volcanology*, *79*(11), 77.

683 Vinciguerra, S., Trovato, C., Meredith, P. G., & Benson, P. M. (2005). Relating seismic velocities, thermal
684 cracking and permeability in Mt. Etna and Iceland basalts. *International Journal of Rock*
685 *Mechanics and Mining Sciences*, *42*(7), 900-910.
686 Wadsworth, F. B., Vasseur, J., Scheu, B., Kendrick, J. E., Lavallée, Y., & Dingwell, D. B. (2016). Universal
687 scaling of fluid permeability during volcanic welding and sediment diagenesis. *Geology*, *44*(3),
688 219-222.
689 Wright, H. M., Cashman, K. V., Gottesfeld, E. H., & Roberts, J. J. (2009). Pore structure of volcanic clasts:
690 measurements of permeability and electrical conductivity. *Earth and Planetary Science*
691 *Letters*, *280*(1), 93-104.
692 Zhang, M., Takahashi, M., Morin, R. H., & Esaki, T. (2000). Evaluation and application of the transient-
693 pulse technique for determining the hydraulic properties of low-permeability rocks—Part 2:
694 experimental application.
695 Zhu, W., Baud, P., Vinciguerra, S., & Wong, T. F. (2016). Micromechanics of brittle faulting and
696 cataclastic flow in Mount Etna basalt. *Journal of Geophysical Research: Solid Earth*, *121*(6),
697 4268-4289.

Table 1. Summary of the experimental data collected for this study. Steady-state permeabilities were collected under a pressure gradient of 0.5 MPa. The pressure gradient at the start of the pulse decay measurements was 0.5 MPa. *Specific surface area of this sample was not measured and is assumed here to be equal to that of sample B5_5. **Specific surface areas of these samples were not measured and are assumed here to be equal to that of another measured sample (EB_7).

Sample	Connected porosity	Specific surface area ($m^2\ kg^{-1}$)	Method	Confining pressure (MPa)	Permeability to water (m^2)	Permeability to gas (m^2)	Permeability to gas / permeability to water	Klinkenberg slip factor, *b* (MPa)	Average pore diameter determined using *b* (μm)
B4_2	0.082	26	steady-state	2	1.09×10^{-15}	1.17×10^{-15}	1.07	0.503	0.054
B5_5	0.085	100	steady-state	2	3.13×10^{-15}	3.97×10^{-15}	1.27	0.069	0.396
A5_11	0.089	15	steady-state	2	1.49×10^{-15}	1.69×10^{-15}	1.13	0.204	0.134
A5_1	0.100	16	steady-state	2	6.55×10^{-15}	7.61×10^{-15}	1.16	0.134	0.204
A5_7	0.137	20	steady-state	2	1.48×10^{-13}	5.14×10^{-13}	3.47	Forchheimer	-
C8_9	0.166	35	steady-state	2	1.04×10^{-13}	5.68×10^{-13}	5.46	Forchheimer	-
C8_8	0.193	28	steady-state	2	6.51×10^{-13}	1.52×10^{-12}	2.33	Forchheimer	-
LAH4_7	0.253	51	steady-state	2	1.34×10^{-12}	2.33×10^{-12}	1.74	Forchheimer	-
LAH4_9	0.267	57	steady-state	2	1.05×10^{-12}	1.76×10^{-12}	1.68	Forchheimer	-
B5_5	0.081	100	steady-state	1	-	5.36×10^{-15}	-	0.054	0.507
B5_5	0.081	100	steady-state	2	-	4.66×10^{-15}	-	0.060	0.456
B5_5	0.081	100	steady-state	5	-	3.65×10^{-15}	-	0.082	0.334
B5_5	0.081	100	steady-state	10	-	2.82×10^{-15}	-	0.100	0.274
B5_5	0.081	100	steady-state	15	-	2.45×10^{-15}	-	0.111	0.246
B5_5	0.081	100	steady-state	20	-	2.23×10^{-15}	-	0.115	0.238
B5_5	0.081	100	steady-state	25	-	2.06×10^{-15}	-	0.120	0.228
B5_5	0.081	100	steady-state	30	-	1.97×10^{-15}	-	0.120	0.228
B5_5	0.081	100	steady-state	35	-	1.79×10^{-15}	-	0.123	0.222
B5_5	0.081	100	steady-state	40	-	1.77×10^{-15}	-	0.119	0.230
B5_5	0.081	100	steady-state	45	-	1.73×10^{-15}	-	0.116	0.236
B5_5	0.081	100	steady-state	50	-	1.73×10^{-15}	-	0.112	0.244
B5_21	0.085	100*	steady-state	1	1.51×10^{-15}	-	-	-	-
B5_21	0.085	100*	steady-state	2	1.33×10^{-15}	-	-	-	-
B5_21	0.085	100*	steady-state	5	1.09×10^{-15}	-	-	-	-
B5_21	0.085	100*	steady-state	10	9.47×10^{-16}	-	-	-	-
B5_21	0.085	100*	steady-state	15	8.55×10^{-16}	-	-	-	-
B5_21	0.085	100*	steady-state	20	7.82×10^{-16}	-	-	-	-
B5_21	0.085	100*	steady-state	25	7.07×10^{-16}	-	-	-	-
B5_21	0.085	100*	steady-state	30	6.82×10^{-16}	-	-	-	-
B5_21	0.085	100*	steady-state	35	6.53×10^{-16}	-	-	-	-
B5_21	0.085	100*	steady-state	40	6.30×10^{-16}	-	-	-	-

B5_21	0.085	100*	steady-state	45	6.02×10^{-16}	-	-	-	-
B5_21	0.085	100*	steady-state	50	5.52×10^{-16}	-	-	-	-
EB_3	0.041	126**	pulse-decay	1	-	8.40×10^{-17}	-	0.096	0.285
EB_3	0.041	126**	pulse-decay	2	-	6.29×10^{-17}	-	0.129	0.212
EB_3	0.041	126**	pulse-decay	5	-	4.83×10^{-17}	-	0.143	0.191
EB_3	0.041	126**	pulse-decay	10	-	3.49×10^{-17}	-	0.162	0.169
EB_3	0.041	126**	pulse-decay	15	-	2.69×10^{-17}	-	0.174	0.157
EB_3	0.041	126**	pulse-decay	20	-	2.14×10^{-17}	-	0.184	0.149
EB_3	0.041	126**	pulse-decay	25	-	1.81×10^{-17}	-	0.187	0.146
EB_3	0.041	126**	pulse-decay	30	-	1.51×10^{-17}	-	0.199	0.137
EB_3	0.041	126**	pulse-decay	35	-	1.31×10^{-17}	-	0.201	0.136
EB_3	0.041	126**	pulse-decay	40	-	1.15×10^{-17}	-	0.206	0.133
EB_3	0.041	126**	pulse-decay	45	-	9.89×10^{-18}	-	0.208	0.131
EB_3	0.041	126**	pulse-decay	50	-	8.73×10^{-18}	-	0.214	0.128
EB_5	0.041	126**	steady-state	1	1.87×10^{-17}	-	-	-	-
EB_5	0.041	126**	steady-state	2	1.53×10^{-17}	-	-	-	-
EB_5	0.041	126**	steady-state	5	1.23×10^{-17}	-	-	-	-
EB_5	0.041	126**	steady-state	10	8.82×10^{-18}	-	-	-	-
EB_5	0.041	126**	steady-state	15	6.70×10^{-18}	-	-	-	-
EB_5	0.041	126**	steady-state	20	5.55×10^{-18}	-	-	-	-
EB_5	0.041	126**	steady-state	25	4.51×10^{-18}	-	-	-	-
EB_5	0.041	126**	steady-state	30	3.70×10^{-18}	-	-	-	-
EB_5	0.041	126**	steady-state	35	3.44×10^{-18}	-	-	-	-
EB_5	0.041	126**	steady-state	40	2.94×10^{-18}	-	-	-	-
EB_5	0.041	126**	steady-state	45	2.46×10^{-18}	-	-	-	-
EB_5	0.041	126**	steady-state	50	2.20×10^{-18}	-	-	-	-

703